

Comparative study of electronic structures and dielectric properties of alumina polymorphs by first-principles methods

Choong-Ki Lee,¹ Eunae Cho,¹ Hyo-Sug Lee,² Kwang Soo Seol,² and Seungwu Han^{1,*}

¹*Department of Physics, Ewha Womans University, Seoul 120-750, Korea*

²*Samsung Advanced Institute of Technology, Suwon 440-600, Korea*

(Received 28 February 2007; revised manuscript received 23 July 2007; published 10 December 2007)

Based on density functional methods, we investigate the origin of variations in electronic structures and dielectric constants of representative alumina polymorphs. We consider the most stable α -Al₂O₃ and three metastable phases of alumina, κ , θ , and γ -Al₂O₃. Computed energy gaps are found to be in the order of $\alpha > \kappa > \theta > \gamma$, which can be understood based on electrostatic potentials at specific lattice sites; while cations occupying tetrahedral sites explain downshifts of conduction bottoms in the metastable alumina, vacant sites in γ -Al₂O₃ account for the gap reduction originated in the valence band. On the other hand, dielectric properties are also calculated based on density functional perturbation methods. On average, the static dielectric constants follow the order of $\kappa > \alpha > \theta > \gamma$. The substantial enhancement of the dielectric constant for κ -Al₂O₃ is attributed to elongated Al-O bonds due to a simultaneous occupation of tetrahedral and octahedral sites by cations within a single layer.

DOI: 10.1103/PhysRevB.76.245110

PACS number(s): 77.84.Bw, 77.22.-d

I. INTRODUCTION

Aluminum oxide (Al₂O₃) or alumina is one of the most important ceramic materials that are widely used in many technological applications such as abrasives, substrates, electrical insulators, tunneling barriers, and catalysts.^{1,2} While the α phase, corundum, is the only stable phase at any pressures or temperatures, there also exist several metastable phases such as β , η , κ , δ , θ , and γ , known as transition alumina.³ The polymorphism of alumina can be classified systematically in terms of the stacking sequence of anions and the distribution pattern of cations in tetrahedral or octahedral interstices. For example, anions in α -Al₂O₃ form the hexagonal-close-packed lattice, while the face-centered cubic arrangement constitutes base structures of anions in θ , γ , δ , and η phases.

Various phases of alumina are dissimilar in physical properties such as the density, dielectric constant, and energy gap, which are closely related to the specific applications of each phase. For example, when used as electrical insulators to replace silicon dioxides in microelectronic devices, it would be desirable to use a phase with high dielectric constants and large energy gaps, such as α -Al₂O₃. While there is a large body of studies on electronic structures and lattice dynamics of individual phases of alumina,⁴⁻¹⁶ less efforts have been directed toward understanding the underlying relationship between atomic structures of polymorphs and their physical properties.¹⁷⁻²³ In this paper, we employ first-principles approaches to compare electronic structures and dielectric constants of α , κ , γ , and θ -Al₂O₃, four representative phases of alumina. Furthermore, we carry out detailed analysis to identify the microscopic origin of variations in the energy gap and dielectric constant from phase to phase.

II. COMPUTATIONAL METHODS AND MODEL SYSTEMS

For a computational framework, we adopt first-principles pseudopotential methods based on density functional theory.

Throughout this work, we use a computational package QUANTUM-ESPRESSO.²⁴ Ion-electron interactions are approximated by ultrasoft pseudopotentials²⁵ to save computational costs and the local density approximation (LDA) is employed for the description of exchange-correlation energies of electrons.²⁶ The wave-function cutoff is chosen to be 40 Ry and k points are sampled in the first Brillouin zone using uniform $4 \times 4 \times 4$, $4 \times 2 \times 2$, $4 \times 4 \times 2$, and $4 \times 4 \times 3$ grids for primitive unit cells of α , κ , γ , and θ -Al₂O₃, respectively. In Ref. 12, the convergence analysis on k -point sampling was carefully carried out for γ -Al₂O₃ by comparing results with $4 \times 4 \times 2$ and $15 \times 15 \times 9$ grids (albeit in a non-self-consistent way) and it was concluded that the $4 \times 4 \times 2$ mesh is sufficient. When we obtain the electronic density of states (DOS), the k -point densities are doubled to locate band edges more accurately. With this choice of computational parameters, the total energy, atomic forces, and stress tensors are converged to within 10^{-3} Ry/at., 2×10^{-3} Ry/Å, and 5 kbar, respectively.

For studying dielectric permittivities, linear response methods based on density functional theory are employed to obtain Born effective charges and phonon modes at zone center.^{27,28} The static dielectric tensors are then calculated according to the following formula:²⁷

$$\varepsilon_{\alpha\beta}^0 = \varepsilon_{\alpha\beta}^\infty + \frac{4\pi}{\Omega} \sum_m \frac{Z_{m\alpha}^* Z_{m\beta}^*}{\omega_m^2}, \quad (1)$$

where $\varepsilon_{\alpha\beta}^\infty$, Ω , and ω_m denote the dielectric tensor contributed by electrons, unit-cell volume, and frequency of the IR-active phonon with a mode number of m , respectively. $Z_{m\alpha}^*$ in Eq. (1) is the mode-projected effective charges defined as follows:

$$Z_{m\alpha}^* = \sum_{k,\beta} \frac{Z_{\alpha\beta}^k u_{m,\beta}^k}{\sqrt{M_k}}, \quad (2)$$

where M_k and $Z_{\alpha\beta}^k$ are the mass and effective charge tensor of atom k , respectively, and $u_{m,\beta}^k$ is the eigenvector of the m th

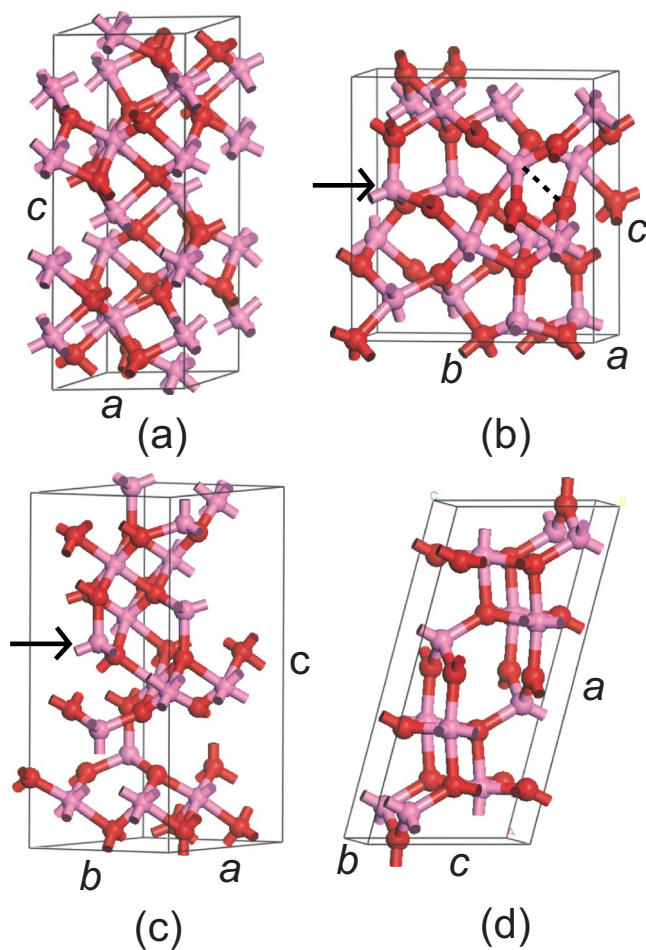


FIG. 1. (Color online) Unit cells of Al_2O_3 studied in this work. (a) $\alpha\text{-Al}_2\text{O}_3$ (hexagonal), (b) $\kappa\text{-Al}_2\text{O}_3$ (orthorhombic), (c) $\gamma\text{-Al}_2\text{O}_3$ (triclinic), and (d) $\theta\text{-Al}_2\text{O}_3$ (monoclinic). The light and dark (red and purple in color) spheres indicate oxygen and aluminum atoms, respectively.

phonon mode. Since we are concerned with static dielectric constants under a homogeneous electric field, i.e., $\varepsilon_{\alpha\beta}(\vec{q}=0, \omega=0)$, the ionic response does not vary from cell to cell. Therefore, only phonon modes at zone center are used in evaluating Eq. (1).

Figure 1 shows unit cells of Al_2O_3 studied in this work. The most stable $\alpha\text{-Al}_2\text{O}_3$ contains two units of Al_2O_3 in rhombohedral representation. Only octahedral sites are occupied in $\alpha\text{-Al}_2\text{O}_3$.²⁹ For a structural model of $\kappa\text{-Al}_2\text{O}_3$ with the anion stacking of $ABAC$ style, we refer to Refs. 14 and 15. On the other hand, the crystal structure of spinel-based γ phase has been a long-standing issue. Recently, an extensive study combining experimental measurements and computational modeling showed that significant portions of nonspinel positions are occupied.⁹ Calculations on such huge models are not feasible within our computational resources and we use a minimal structure containing 40 atoms derived from the spinel as proposed in Ref. 11. In defective spinel structures, the most stable configuration was obtained when two vacancies at octahedral sites are farthest from each other.²⁰ Lastly, our model of $\theta\text{-Al}_2\text{O}_3$ is based on the structure used

in Refs. 16 and 21. It contains alternating layers of cations occupying either tetrahedral or octahedral sites.

III. RESULTS AND DISCUSSIONS

A. Structural properties

In Table I, computational results on equilibrium lattice parameters are shown with comparison to experimental or other theoretical results when available. The overall agreements are satisfactory. Other bulk properties are compiled in Table II. It is seen that the equilibrium volume increases monotonically with the ratio of tetrahedral to octahedral sites occupied by Al atoms ($N_{\text{tet}}/N_{\text{oct}}$). This is understandable since one of the Al-O bonds around Al atom at tetrahedral sites (Al_{tet}) points along the direction of anion stacking, which in turn expands layer-to-layer distances. On the other hand, it is found that the equilibrium energy is not simply dependent on $N_{\text{tet}}/N_{\text{oct}}$. It is believed that positional disorders in $\gamma\text{-Al}_2\text{O}_3$ further increase the energy. An interesting observation is that the total energy is well correlated with the energy gap.

For a comparison purpose, we also calculate on alumina with the hypothetical bixbyite structure which is generally preferred for larger sizes of cations such as Lu_2O_3 .^{22,23} Most empirical potentials for alumina are known to favor the bixbyite structure over corundum. It was suggested that corundum became more stable than the bixbyite phase if the quadrupolar polarizability of oxygen ions is considered in the shell model.²² In the last line of Table II, the computed properties of the bixbyite Al_2O_3 are shown. It is seen that the structure is surprisingly stable with a total energy close to that of the κ phase, partly explaining the difficulties in the empirical modeling. The energy gap and dielectric constants are also comparable to those in other phases.

B. Electronic structures

In Fig. 2, the total and partial DOSs are displayed. The basic features are shared by all phases. That is to say, O $2s$ bands are lowest in energy (not shown in the figure) and valence bands shown in Fig. 2 consist mainly of O $2p$ orbitals, slightly intermixed with Al $3s$ and Al $3p$ orbitals. While lower and middle parts of the valence bands show an indication of covalent bonding between O and Al atoms, the upper part mostly consists of O $2p$ orbitals. The absence of Al states in these energy ranges can be interpreted as a non-bonding nature of O $2p$ orbitals. On the other hand, it is found that conduction bands in Fig. 2 are decomposed into O $2s$ and Al $3s$ states, with a small addition of O $2p$ characters. To examine the dependence of DOS on structural models for $\gamma\text{-Al}_2\text{O}_3$, a larger model suggested in Ref. 11 which includes 32 units of Al_2O_3 was also calculated; however, it is found that overall distributions of DOS are similar to that of the smaller model in Fig. 2(c).

As shown in Table II, the calculated energy gaps are in the order of $\alpha > \kappa > \theta > \gamma$, with $\alpha\text{-Al}_2\text{O}_3$ exhibiting the largest energy gap. The widths of valence bands in Fig. 2 are 7.13, 7.11, 8.6, and 7.0 eV for α , κ , γ , and θ phases, respectively. The largest width for $\gamma\text{-Al}_2\text{O}_3$ is attributed to the rise of the

TABLE I. Structural parameters for various phases of alumina at equilibrium (see Fig. 1). Only nontrivial parameters (noted in parentheses under each phase name) are shown. All lengths are in angstroms. GGA represents generalized gradient approximations.

Phase	This work	Other calculations	Expt.
α (a, c)	(4.70, 12.84)	(4.77, 12.97) ^a (4.70, 12.83) ^c (4.78, 13.05) ^d (4.75, 13.10) ^e	(4.76, 13.00) ^b
κ (a, b, c)	(4.78, 8.21, 8.82)	(4.80, 8.26, 8.88) ^f (4.80, 8.25, 8.88) ^h	(4.84, 8.33, 8.95) ^g
γ (a, b, c α, β, γ)	(5.56, 5.53, 13.36 89.4°, 90.1°, 120.2°)	(5.56, 5.57, 13.48 89.3°, 90.0°, 120.2°) ⁱ	N/A
θ (a, b, c, β)	(11.58, 2.88, 5.57, 104.3°)	(11.69, 2.91, 5.62, 103.9°) ^j (11.85, 2.92, 5.63, 104.0°) ^d	(11.80, 2.91, 5.62, 103.8°) ^k (11.85, 2.90, 5.62, 103.8°) ^l

^aReference 12 (LDA, all electron+Gaussian basis).

^bReference 23.

^cReference 4 (LDA, pseudopotential+mixed basis).

^dReference 8 (GGA, pseudopotential+plane wave basis).

^eReference 30 (shell model including dipole and quadrupole polarizabilities).

^fReference 10 (LDA, pseudopotential+plane wave basis).

^gReference 24.

^hReference 25 (LDA, pseudopotential+plane wave basis).

ⁱReference 15 (LDA, pseudopotential+plane wave basis).

^jReference 17 (Hartree-Fock).

^kReference 27.

^lReference 28.

valence edge and accounts for the smallest energy gap among calculated polymorphs. To explain this, we inspect the spatial distribution of wave functions at the valence top of γ -Al₂O₃ and it is identified as O 2*p* orbitals surrounding vacant sites in the defective spinel structure. In addition, the analysis on electrostatic potentials shows that the potential values averaged within 1.4 Å around those oxygen atoms are substantially higher than for other oxygen sites by 0.6–1.5 eV. Based on these observations, the rising of the valence edge in γ -Al₂O₃ can be understood as follow: positively ionized cations are a source of attractive potentials for electrons. Therefore, the absence of cations at defect sites effectively increases nearby electrostatic potentials, which in

turn raises the on-site energy of nonbonding O 2*p* orbitals forming the bands near the valence top.

On the other hand, downshifts of the conduction bottom are responsible for the band-gap reduction for all metastable phases, implying that the occupation of Al atoms at tetrahedral sites is a primary reason. To enlighten this, we examine states at the conduction bottom of each phase as shown in Fig. 3. It is noticeable that charge densities for κ , γ , and θ -Al₂O₃ are substantially polarized toward Al_{tet}. This can be understood based on bonding distances. The atomic structures at equilibrium show that Al-O bonds around octahedral sites are longer than those in tetrahedral sites by 0.1–0.2 Å. A slight hybridization of O 2*s* states with O 2*p* orbitals

TABLE II. Computed physical properties for various phases of alumina. N_{oct} (N_{tet}) is the number of atoms at octahedral (tetrahedral) sites. V_0 and E_{tot} are the volume and energy per formula unit, respectively. The latter is referenced to that of α -Al₂O₃. E_g is the fundamental energy gap, and $\overline{\epsilon_\infty}$ and $\overline{\epsilon_0}$ indicate averaged optical and static dielectric constants, respectively.

Phase	Anion packing	$N_{\text{oct}}:N_{\text{tet}}$	V_0 (Å ³)	E_{tot} (eV)	E_g (eV)	$\overline{\epsilon_\infty}$	$\overline{\epsilon_0}$
α	AB	1:0	40.99	0.00	6.72	3.17	9.72
κ	ABAC	3:1	43.28	0.21	5.49	3.15	10.99
γ	ABC	5:3	44.35	0.37	4.40	3.11	8.48
θ	ABC	1:1	45.04	0.25	5.04	3.13	8.52
Bixbyite			42.28	0.21	5.83	3.15	9.31

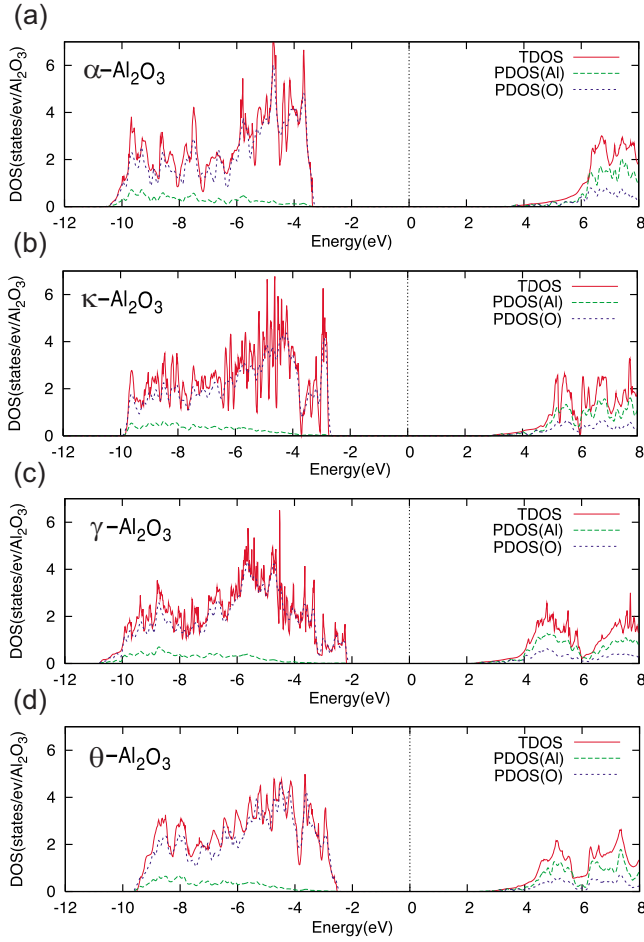


FIG. 2. (Color online) Total and partial densities of states (TDOS and PDOS, respectively) onto Al or O atoms. The Fermi level is set to zero (vertical dotted lines).

moves charge centers toward more attractive potentials at the tetrahedral sites, and thereby O $2s$ orbitals become more stable and the conduction bottom shifts down. On the other hand, the O $2s$ orbital in α - Al_2O_3 is also polarized but it is not pointing to any of four nearby cations at octahedral sites (Al_{oct}).

C. Dielectric properties

Next, we compare dielectric properties between polymorphs using the density functional perturbation method outlined in Sec. II. The computed Born effective charges are found to vary less than 10% from phase to phase, implying that charge transfers are similar among polymorphs. In Table III, we enlist all phonon modes at zone center obtained from the calculations. The space groups of the model systems are $R3c$, $Pna2_1$, $C2/m$, and $C2/m$ for α , κ , γ , and θ - Al_2O_3 , respectively. (We recall that the γ phase belongs to $Fd3m$ experimentally.²⁸) According to a standard group-theoretical analysis, the irreducible representations of phonon modes are obtained as follows:

$$\Gamma_{\text{vib}}^{\alpha} = 2A_{1g} \oplus 2A_{1u} \oplus 3A_{2g} \oplus 3A_{2u} \oplus 5E_g \oplus 5E_u, \quad (3)$$

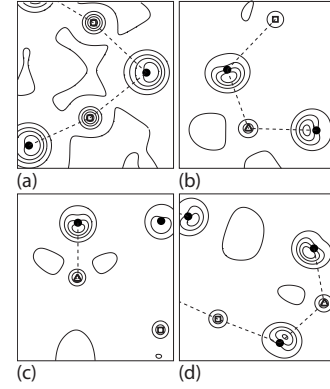


FIG. 3. Contour plots of the squared wave functions corresponding to the conduction bottom at Γ point. (a) α - Al_2O_3 , (b) κ - Al_2O_3 , (c) γ - Al_2O_3 , and (d) θ - Al_2O_3 . $(1\bar{1}0)$ planes are chosen for (a), (b), and (d). For the γ - Al_2O_3 in (c), the contours are drawn on a plane parallel to (010) . Filled circles are oxygen atoms, and empty squares and triangles indicate cations at octahedral and tetrahedral sites, respectively. The contour spacing is 0.004 , $0.006 e/a.u.^3$ in (a) and (d), respectively, and $0.0016 e/a.u.^3$ in (b) and (c).

$$\Gamma_{\text{vib}}^{\kappa} = 30A_1 \oplus 30A_2 \oplus 30B_1 \oplus 30B_2, \quad (4)$$

$$\Gamma_{\text{vib}}^{\gamma} = 34A_g \oplus 26A_u \oplus 23B_g \oplus 37B_u, \quad (5)$$

$$\Gamma_{\text{vib}}^{\theta} = 10A_g \oplus 5A_u \oplus 5B_g \oplus 10B_u. \quad (6)$$

The agreements between phonon modes in Table III and previous experimental data for the α phase or theoretical data for the κ phase are within 3%.^{4,8} On the other hand, our data for the α phase are larger by 5% than theoretical estimations in Ref. 4, which is attributable to using different first-principles approaches. It is noted that our data slightly overestimate experimental measurements while results in Ref. 4 underestimate them by almost same amounts.

Table II shows the dielectric constants computed according to Eq. (1) using IR-active phonon modes in Table III and Born effective charges. It is intriguing that ε_{∞} , averaged optical dielectric constants, scales with the energy gap, although differences are small. This is at variance with a general perception that materials with a larger band gap tend to show smaller ε_{∞} . On the other hand, there exist substantial variations in the ionic response, and hence in the static dielectric permittivity, among the polymorphs. The anisotropies in $\varepsilon_0^{\text{ion}}$ are within 10%, except for α - Al_2O_3 where $\varepsilon_0^{\text{ion}}$ along the c axis is larger than those for in-plane directions by 35%. The smallest values of the energy gap as well as the dielectric constant are obtained for γ - Al_2O_3 . This contrasts with its application to replacement gate oxides where opposite properties are strongly required.³⁰

In Table II, it is also noticeable that ε_0 for κ - Al_2O_3 is largest among polymorphs considered in this work. The computed value agrees well with the previous literature.⁸ In order to reveal the microscopic origin to enhance the dielectric constant, we plot $\varepsilon_0^{\text{ion}}(\omega)$ in Fig. 4 defined as follows.

TABLE III. Phonon frequencies (f) for mode number n at zone center. The phonon modes are sorted in the order of increasing frequencies. The representation for each mode is noted in parentheses. Frequencies are in cm^{-1} .

n	f	n	f	n	f	n	f	n	f
$\alpha\text{-Al}_2\text{O}_3$ (IR active: A_{2u} and E_u , Raman active: A_{1g} and E_g , translational modes: A_{2u} and E_u)									
1	316.4 (A_{2g})	7	427.0 (A_{1g})	13	453.2 (E_g)	19	595.2 (A_{2u})	25	761.8 (A_{2g})
2	382.4 (E_g)	8	443.5 (E_g)	14	537.9 (A_{2g})	20	606.5 (A_{1u})	26	762.3 (E_g)
3	382.4 (E_g)	9	443.5 (E_g)	15	582.1 (E_g)	21	644.5 (E_u)	27	762.3 (E_g)
4	394.0 (E_u)	10	448.7 (E_u)	16	582.1 (E_g)	22	644.5 (E_u)		
5	394.0 (E_u)	11	448.7 (E_u)	17	585.6 (E_u)	23	653.8 (A_{1g})		
6	404.2 (A_{2u})	12	453.2 (E_g)	18	585.6 (E_u)	24	700.7 (A_{1u})		
$\kappa\text{-Al}_2\text{O}_3$ (IR active: A_1 , B_1 , and B_2 , Raman active: A_1 , A_2 , B_1 , and B_2 , translational modes: A_1 , B_1 , and B_2)									
1	140.1 (A_1)	25	322.6 (B_2)	49	453.1 (B_1)	73	562.1 (A_2)	97	741.6 (A_2)
2	149.7 (A_2)	26	324.6 (A_1)	50	460.6 (A_1)	74	568.8 (A_1)	98	744.2 (A_1)
3	176.7 (B_1)	27	329.7 (B_2)	51	460.6 (B_2)	75	568.8 (A_2)	99	745.6 (B_2)
4	179.6 (A_2)	28	330.4 (B_1)	52	468.2 (A_2)	76	569.7 (B_2)	100	753.9 (B_1)
5	191.0 (B_2)	29	338.6 (B_1)	53	469.2 (B_1)	77	573.9 (B_2)	101	754.2 (A_1)
6	193.2 (A_1)	30	343.4 (A_2)	54	470.6 (B_2)	78	582.1 (A_1)	102	769.8 (A_2)
7	202.5 (B_1)	31	347.3 (A_1)	55	480.2 (A_2)	79	599.9 (B_1)	103	775.7 (B_2)
8	209.3 (A_1)	32	359.8 (A_2)	56	482.9 (A_1)	80	601.3 (B_2)	104	779.9 (B_1)
9	222.0 (A_2)	33	359.9 (B_1)	57	486.1 (A_2)	81	618.4 (A_2)	105	785.4 (A_2)
10	233.1 (B_2)	34	363.5 (B_1)	58	488.4 (B_2)	82	625.4 (A_1)	106	786.7 (B_1)
11	246.3 (A_2)	35	366.2 (B_2)	59	493.4 (A_2)	83	628.9 (A_1)	107	791.2 (B_2)
12	252.8 (A_1)	36	370.3 (A_2)	60	496.2 (B_1)	84	630.1 (B_2)	108	796.6 (A_1)
13	254.0 (B_1)	37	385.5 (B_2)	61	504.3 (A_1)	85	635.6 (B_1)	109	798.7 (A_1)
14	268.1 (B_2)	38	401.1 (A_2)	62	505.3 (B_1)	86	642.4 (A_2)	110	820.0 (B_2)
15	273.4 (A_2)	39	404.7 (B_2)	63	508.5 (A_2)	87	650.8 (B_1)	111	823.7 (B_1)
16	278.6 (A_1)	40	405.4 (A_1)	64	512.2 (A_1)	88	664.6 (B_2)	112	826.9 (A_2)
17	289.7 (A_1)	41	406.7 (B_1)	65	513.2 (B_2)	89	677.6 (A_1)	113	838.6 (B_1)
18	294.3 (B_1)	42	412.9 (B_1)	66	535.2 (A_1)	90	677.7 (A_2)	114	845.4 (B_2)
19	298.8 (B_2)	43	419.8 (A_2)	67	535.7 (B_2)	91	695.3 (B_1)	115	849.8 (A_1)
20	299.4 (A_2)	44	420.2 (A_1)	68	543.8 (B_1)	92	704.0 (B_2)	116	868.9 (A_2)
21	303.1 (B_2)	45	425.2 (B_2)	69	548.4 (B_2)	93	711.4 (A_2)	117	922.3 (B_1)
22	303.9 (B_1)	46	425.7 (B_1)	70	554.5 (A_1)	94	717.3 (B_2)		
23	313.1 (A_1)	47	426.6 (A_1)	71	555.2 (A_2)	95	728.3 (A_2)		
24	316.2 (A_2)	48	440.9 (B_1)	72	558.1 (B_1)	96	734.1 (A_1)		
$\gamma\text{-Al}_2\text{O}_3$ (IR active: A_u , and B_u , Raman active: A_g , and B_g , translational modes: B_u , B_u , and A_u)									
1	99.3 (A_g)	25	322.1 (A_u)	49	437.7 (A_g)	73	588.4 (B_g)	97	690.7 (A_g)
2	105.5 (B_g)	26	328.4 (B_u)	50	440.8 (B_g)	74	591.1 (B_u)	98	691.6 (B_g)
3	139.5 (A_u)	27	330.5 (A_g)	51	452.5 (B_u)	75	591.5 (A_u)	99	693.6 (B_u)
4	139.9 (B_u)	28	331.0 (B_g)	52	469.5 (A_g)	76	594.6 (B_g)	100	704.7 (A_g)
5	201.6 (A_g)	29	342.7 (A_g)	53	470.9 (A_u)	77	595.4 (A_u)	101	715.6 (B_u)
6	211.8 (B_g)	30	345.8 (A_u)	54	480.0 (B_u)	78	599.5 (A_g)	102	759.7 (B_u)
7	233.4 (A_g)	31	346.6 (B_u)	55	481.2 (B_g)	79	608.1 (A_u)	103	769.1 (A_g)
8	236.4 (A_u)	32	351.9 (B_g)	56	498.9 (A_g)	80	609.8 (A_g)	104	779.2 (B_u)
9	240.7 (B_u)	33	354.8 (A_g)	57	502.4 (A_u)	81	612.1 (B_u)	105	797.7 (A_g)
10	253.3 (B_g)	34	364.5 (A_g)	58	506.5 (B_u)	82	614.3 (B_g)	106	813.7 (A_u)
11	261.2 (A_u)	35	375.3 (B_u)	59	507.3 (A_g)	83	620.4 (B_u)	107	816.6 (B_g)
12	264.2 (A_u)	36	381.5 (A_u)	60	511.0 (A_u)	84	632.7 (A_u)	108	817.5 (A_u)

TABLE III. (*Continued.*)

n	f	n	f	n	f	n	f	n	f
13	270.2 (B_u)	37	387.6 (B_g)	61	513.0 (B_g)	85	635.1 (B_u)	109	818.7 (B_u)
14	271.1 (A_g)	38	390.1 (A_g)	62	518.9 (B_u)	86	638.0 (B_u)	110	819.2 (B_g)
15	274.7 (B_g)	39	393.9 (A_u)	63	528.4 (A_u)	87	639.2 (A_g)	111	821.2 (A_g)
16	280.1 (A_u)	40	403.7 (B_u)	64	529.7 (B_u)	88	648.8 (B_g)	112	826.2 (B_u)
17	281.2 (B_u)	41	406.5 (A_g)	65	535.6 (B_u)	89	649.3 (A_g)	113	845.8 (A_g)
18	287.4 (A_g)	42	407.1 (B_u)	66	543.2 (A_g)	90	651.0 (A_u)	114	857.6 (B_u)
19	298.3 (B_g)	43	410.3 (B_g)	67	557.5 (A_g)	91	651.7 (B_u)	115	888.6 (A_g)
20	305.2 (B_u)	44	411.0 (A_u)	68	565.6 (B_g)	92	657.8 (A_g)	116	910.4 (A_g)
21	310.0 (A_u)	45	419.3 (A_g)	69	572.4 (B_u)	93	664.9 (B_u)	117	924.2 (B_u)
22	314.2 (B_u)	46	421.0 (B_g)	70	577.0 (A_g)	94	669.9 (A_u)		
23	317.3 (A_g)	47	423.1 (B_u)	71	579.7 (B_g)	95	673.6 (B_u)		
24	319.3 (B_g)	48	428.8 (A_u)	72	582.9 (A_u)	96	685.8 (A_g)		
θ -Al ₂ O ₃ (IR active: A_u , and B_u , Raman active: A_g , and B_g , translational modes: B_u , B_u , and A_u)									
1	193.2 (B_g)	7	310.2 (B_u)	13	475.6 (A_g)	19	622.2 (A_g)	25	797.2 (A_u)
2	207.6 (A_g)	8	347.5 (B_u)	14	518.7 (A_u)	20	688.1 (B_u)	26	832.2 (B_u)
3	239.0 (A_g)	9	364.5 (A_u)	15	525.7 (B_u)	21	749.5 (A_g)	27	844.5 (A_g)
4	252.7 (B_g)	10	411.5 (B_g)	16	540.1 (B_g)	22	761.7 (B_u)		
5	272.3 (A_u)	11	444.6 (A_g)	17	577.9 (A_g)	23	777.1 (A_g)		
6	295.5 (A_g)	12	453.0 (B_u)	18	590.0 (B_u)	24	790.8 (B_g)		

$$\overline{\varepsilon}_0^{ion}(\omega) = \frac{4\pi}{3\Omega} \sum_{\alpha,m}^{\omega_m < \omega} \frac{Z_{m\alpha}^* Z_{m\alpha}}{\omega_m^2}. \quad (7)$$

By considering phonon modes with frequencies below ω , the plot helps us to resolve contributions to the dielectric permittivity in terms of phonon frequencies. In Fig. 4, it is seen that low-frequency components are mainly responsible for the enhancement of ε_0 in κ -Al₂O₃. From a detailed inspection of the IR-active modes in κ -Al₂O₃, we find that a pair of elongated Al-O bonds is the main source of the large dielectric response at low frequencies. One of them is indicated by a dashed line in Fig. 1(b). These Al-O bonds are related to a simultaneous presence of Al_{oct} and Al_{tet} within a single cation layer which we call a “mixed” layer [see the arrow in Fig. 1(b)]. As mentioned above, Al_{tet} tends to in-

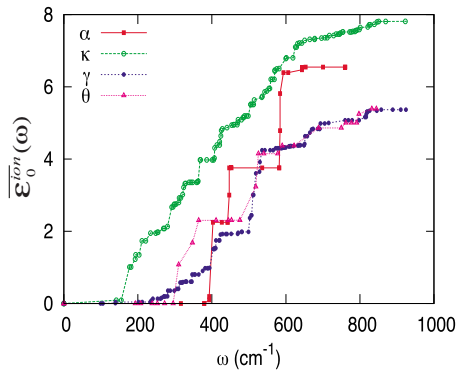


FIG. 4. (Color online) The averaged, static dielectric constants contributed by phonons with frequencies below ω

crease distances between sandwiching anion layers. As a consequence, one of the Al-O bonds around Al_{oct} in the mixed layer is elongated with its length increased to 2.2 Å, compared to typical Al_{oct}-O bonds of 1.8–1.9 Å. The weakened Al-O bonds are easily polarized with large ionic motions, which in turn increase the static dielectric constants. On the other hand, there are also mixed layers in γ -Al₂O₃ where two-thirds of cations occupy tetrahedral sites [see the arrow in Fig. 1(c)]. However, the cation layer right above the mixed layer contains vacant sites, and oxygen atoms can relax to maintain the Al-O bond lengths around Al_{oct}. This is contrasted to κ -Al₂O₃ where the mixed layer is sandwiched between cation layers with purely octahedral occupations.

IV. SUMMARY

In summary, we have studied electronic structures and dielectric responses of four representative phases of Al₂O₃. The energy gap is in the order of $\alpha > \kappa > \theta > \gamma$ and the averaged, static dielectric constant follows the order of $\kappa > \alpha > \theta > \gamma$. Two underlying mechanisms were identified for the reduction of energy gap for metastable phases; firstly, the higher electrostatic potential around vacant sites accounts for the smallest energy gap of γ -Al₂O₃. Secondly, the orbital energy was found to be lower for oxygen atoms around the tetrahedral sites in metastable phases compared to octahedral sites, explaining the downshifts of conduction bottoms. On the other hand, the enhancement of dielectric permittivity for κ -Al₂O₃ originated from softened Al-O bonds in a mixed cation layer where Al atoms occupy both octahedral and tetrahedral sites.

ACKNOWLEDGMENTS

This work was supported by Samsung Electronics and the System IC 2010 program of the Korean government. The

computations were carried out at Korea Institute of Science and Technology Information (KISTI) through Eighth Strategic Supercomputing Program.

*Author to whom correspondence should be addressed; hansw@ewha.ac.kr

- ¹W. H. Gitzen, *Alumina as a Ceramic Material* (American Ceramic Society, Columbus, OH, 1970), Special Publication No. 4.
- ²E. Dörre and H. Hübner, *Alumina* (Springer-Verlag, Berlin, 1984).
- ³I. Levin and D. Brandon, *J. Am. Ceram. Soc.* **81**, 1995 (1995).
- ⁴R. Heid, D. Strauch, and K.-P. Bohnen, *Phys. Rev. B* **61**, 8625 (2000).
- ⁵W. Y. Ching and Yong-Nian Xu, *J. Am. Ceram. Soc.* **77**, 404 (1994).
- ⁶Y. Yourdshahyan, C. Ruberto, L. Bengtsson, and B. I. Lundqvist, *Phys. Rev. B* **56**, 8553 (1997).
- ⁷R. Ahuja, J. M. Osorio, J. Almeida, B. Holm, W. Y. Ching, and B. Johansson, *J. Phys.: Condens. Matter* **16**, 2891 (2004).
- ⁸R. Vali and S. Hosseini, *Comput. Mater. Sci.* **29**, 138 (2004).
- ⁹G. Paglia, A. L. Rohl, C. E. Buckley, and J. D. Gale, *Phys. Rev. B* **71**, 224115 (2005).
- ¹⁰J. C. Boettger, *Phys. Rev. B* **55**, 750 (1997).
- ¹¹G. Gutiérrez, A. Taga, and B. Johansson, *Phys. Rev. B* **65**, 012101 (2001).
- ¹²E. Menéndez-Proupin and G. Gutiérrez, *Phys. Rev. B* **72**, 035116 (2005).
- ¹³A. P. Borosy, B. Silvi, and M. Allavena, *J. Phys. Chem.* **98**, 13189 (1994).
- ¹⁴B. Ollivier, R. Retoux, P. Lacorre, D. Massiot, and G. Férey, *J. Mater. Chem.* **7**, 1049 (1997).
- ¹⁵Y. Yourdshahyan, C. Ruberto, M. Halvarsson, L. Bengtsson, V. Langer, B. I. Lundqvist, S. Rупpi, and U. Rolander, *J. Am. Ceram. Soc.* **82**, 1365 (1999).
- ¹⁶E. Husson and Y. Repelin, *Eur. J. Solid State Inorg. Chem.* **33**, 1223 (1996).
- ¹⁷S. D. Mo and W. Y. Ching, *Phys. Rev. B* **57**, 15219 (1998).
- ¹⁸Z. Łodziana and K. Parliński, *Phys. Rev. B* **67**, 174106 (2003).
- ¹⁹S.-H. Cai, S. N. Rashkeev, S. T. Pantelides, and K. Sohlberg, *Phys. Rev. Lett.* **89**, 235501 (2002).
- ²⁰C. Wolverton and K. C. Hass, *Phys. Rev. B* **63**, 024102 (2000).
- ²¹R. S. Zhou and R. L. Snyder, *Acta Crystallogr., Sect. B: Struct. Sci.* **47**, 617 (1991).
- ²²M. Wilson, M. Exner, Y.-M. Huang, and M. W. Finnis, *Phys. Rev. B* **54**, 15683 (1996).
- ²³S. D. Kenny, D. Nguyen-Manh, H. Fujitani, and A. P. Sutton, *Philos. Mag. Lett.* **78**, 469 (1998).
- ²⁴<http://www.pwscf.org>
- ²⁵D. Vanderbilt, *Phys. Rev. B* **41**, 7892 (1990).
- ²⁶D. M. Ceperley and B. J. Alder, *Phys. Rev. Lett.* **45**, 566 (1980).
- ²⁷X. Gonze and C. Lee, *Phys. Rev. B* **55**, 10355 (1997).
- ²⁸S. Baroni, S. de Gironcoli, and A. D. Corso, *Rev. Mod. Phys.* **73**, 515 (2001) and references therein.
- ²⁹R. W. G. Wyckoff, *Crystal Structures*, 2nd ed. (Interscience, New York, 1964), Vol. 2, p. 6.
- ³⁰C. Merckling, M. El-Kazzi, G. Delhaye, M. Gendry, G. Saint-Girons, L. Largeau, and G. Patriarche, *Appl. Phys. Lett.* **89**, 232907 (2006).